Topological Phase Transformation and Collapse Dynamics of Spin Textures in a Non-Centrosymmetric D_{2d} System

Jagannath Jena,* Sabri Koraltan, Florian Bruckner, Konstantin Holst, Malleswararao Tangi, Claas Abert, Claudia Felser, Dieter Suess, and Stuart S.P. Parkin*

Recently a large variety of non-collinear spin textures have been revealed in various crystals with different symmetry groups. Of particular interest are crystals with D_{2d} symmetry that exhibit a complex variety of stable and metastable spin textures that includes antiskyrmions, elliptical Bloch-skyrmions, fractional-antiskyrmions, fractional Bloch-skyrmions, and type-II trivial-bubbles. The observation of these structures necessitates their stabilization via magnetic field and temperature protocols which demands a thorough understanding of their creation, transformation, and collapse dynamics. Utilizing the real-space imaging capabilities of Lorentz transmission electron microscopy, the generation and annihilation of diverse spin textures in a single D_{2d} Heusler compound are demonstrated. It is showed that antiskyrmions and elliptical Bloch-skyrmions can be deformed into more elaborate elongated magnetic nano-objects through a collapse mechanism. Their elongation is governed by the intrinsic antisymmetric Dzyaloshinskii-Moriya vector exchange interaction and dipolar energy present in the system. Furthermore, antiskyrmions are found to be metastable at all temperatures on field-cooling, while a topological phase transformation from elliptical Bloch-skyrmions to antiskyrmions rather takes places on field-heating. These results are corroborated by micromagnetic simulations and demonstrate the efficient manipulation of different spin textures in a D_{2d} compound by varying field and temperature protocols and represents a critical step toward the application of magnetic skyrmions.

1. Introduction

In most ferro- and ferri-magnetic materials the Heisenberg exchange interaction gives rise to collinear magnetic states in which the magnetic moments are oriented either parallel or anti-parallel to one another. On the other hand the Dzyaloshinskii-Moriya vector exchange interaction (DMI) aligns neighboring moments perpendicular to one another in a chiral manner, thereby encouraging the formation of chiral helical or cycloidal magnetization textures.[1] On applying a magnetic field to such a helical phase, nanoscopic vortex-like textures known as skyrmions may form. These objects have been proposed as potential magnetic bits for memory and logic applications.[2–4] Skyrmions were discovered initially in the cubic B20 compound MnSi that has a chiral crystal structure.[5] Subsequently, a zoology of spin textures have been uncovered in several other B20 compounds,[6–8] as well as in compounds with other crystal symmetries including C_{nv},[9,10] D_{2d},[11,12] and S_4[13] symmetries. In all these cases the DMI interaction arises from the bulk

J. Jena[+], K. Holst, M. Tangi, S. S. Parkin
Max Planck Institute of Microstructure Physics
06120 Halle, Germany
E-mail: jagannath.jena@mpi-halle.mpg.de;
stuart.parkin@mpi-halle.mpg.de

S. Koraltan, F. Bruckner, C. Abert, D. Suess
Physics of Functional Materials
Faculty of Physics
University of Vienna
Vienna 1090, Austria

S. Koraltan
Vienna Doctoral School in Physics
University of Vienna
Vienna 1090, Austria

K. Holst
Institute of Physics
Martin Luther University Halle- Wittenberg
06120 Halle (Saale), Germany

C. Abert, D. Suess
Research Platform MMM Mathematics-Magnetism-Materials
University of Vienna
Vienna 1090, Austria

C. Felser
Max Planck Institute for Chemical Physics of Solids
01187 Dresden, Germany

ADVANCED
SCIENCE NEWS
www.advancedsciencenews.com

ADVANCED
FUNCTIONAL
MATERIALS
www.afm-journal.de

crystal structure. On the other hand, chiral skyrmion-like magnetic bubbles have been observed in multilayered hetero-structures that are stabilized by an interface DMI.[14,15] Such spin textures derived from both bulk and interface DMI can be quantified by their topological charge $N_{SK} = \frac{1}{4\pi} \iint \mathbf{m}(\mathbf{r}) \cdot (\frac{\partial \mathbf{m}(\mathbf{r})}{\partial x} \times \frac{\partial \mathbf{m}(\mathbf{r})}{\partial y})\, d^2r$, where $\mathbf{m}$ is the normalized magnetization vector field.[16,17] N_{SK} takes only integer values except for one case where spin textures with a fractional charge have been reported.[18]

The form of the DMI vector reflects the symmetry of the crystal structures and, thereby, determines which type (or types in a few cases) of spin textures are possible. For example, in compounds with B20, C_{nv}, D_{2d}, or S_4 symmetries, the DMI vector exchange interaction allows for the formation of Bloch, Néel, and antiskyrmions (aSk), respectively.[1,19] It is the competition between the DMI and Heisenberg exchange interactions, the perpendicular magnetic anisotropy, long-range dipole-dipole interactions (DDI), and external field that determines the detailed nature and size of the skyrmionic spin textures and their formation into, for example, hexagonal or square lattices. The dipolar interaction appears to play little role in the B20 compounds[20–23] but is responsible for the large variation in size of the aSks in D_{2d} materials[24] and the Néel skyrmions in C_{nv} compounds[25] as the thickness of lamellae of the host compound is varied. Furthermore, due to the interplay between DMI and DDI, several novel spin textures including, elliptical Bloch skyrmions (eBSks), fractional antiskyrmions (faSks), fractional Bloch skyrmions (fB-Sks), and type-II trivial bubbles (TBs) have been found in the same D_{2d} compound.[18,26,27] The simultaneous presence of these distinct spin objects is an important step forward in developing multi-bit racetrack storage devices.[28]

The control and application of skyrmionic spin textures necessitates a detailed understanding of how an applied magnetic field and temperature and their history influences their formation. In this study, we examine the detailed evolution of the various spin textures in the archetypal D_{2d} compound $Mn_{1.4}Pt_{0.9}Pd_{0.1}Sn$ as a function of magnetic field, temperature, and prior magnetic states. The stable magnetic state of this compound in large magnetic fields, like most magnetic Heusler compounds, is a ferrimagnetic state where two Mn sub-lattices, in which the Mn moments are aligned parallel to one another, are oriented antiparallel to one another. The different moments on the sub-lattices that are formed from Mn in two distinct Wyckoff crystal sites lead to a net magnetization.[29] We show how the stability region of the different skyrmionic nano-objects can be significantly modified based on the initial magnetic state and subsequent applications of magnetic field and temperature. It is found that when driven by an external magnetic field, aSks and eBSks can experience significant deformations and merge with the nearest objects to generate elongated aSks or eBSks, ultimately transforming into the helical state, defining the "collapse dynamics". Extensive field-cooled and field-heated studies that are conducted across a temperature range from 100 to 355 K, reveal the stability and the transformation between spin textures; we observe that aSks remain metastable throughout, while in field-heated experiments, eBSks can be transformed into aSks. Moreover, we have carried 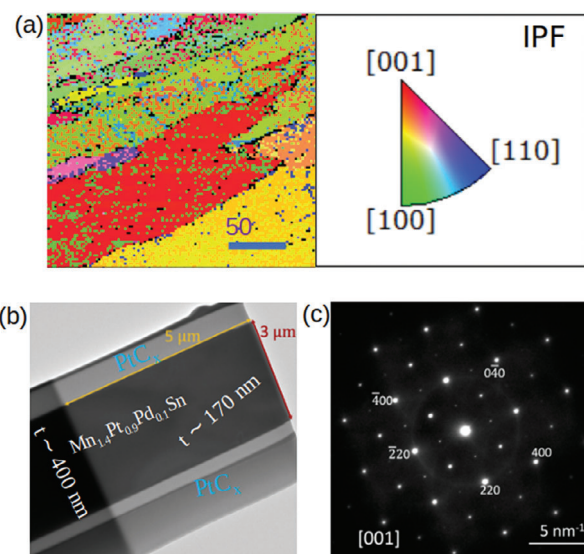out micromagnetic simulations which are in good agreement with our LTEM investigations of the collapse dynamics, metastability, and transformation of eBSks and aSks.

Figure 1. D_{2d} Heusler compound Mn-Pt-Pd-Sn. a) Electron back-scattered image of a polycrystalline bulk compound Mn-Pt-Pd-Sn. The [001] and [100] orientations are illustrated schematically near to the right side of (a). The inverse pole figure (IPF) helps to identify the crystal orientations. b) A thin specimen is lifted from the red-colored region of (a) and a transmission electron microscopy (TEM) overview is shown here. The length, width, and thickness of the electron transparent region of the lamella are ≈ 5 µm, 3 µm, and 170 nm, respectively. Outside of the 5×3 µm^2 region is the PtC_x, which was deposited during the specimen preparation in a focused ion beam (FIB) as a protection layer. c) The selected area electron diffraction (SAED) pattern is obtained from the 170 nm thick region, showing the [001] orientation.

2. Results and Discussion

Using an arc-melting technique large ingots of the bulk Heusler compound $Mn_{1.4}Pt_{0.9}Pd_{0.1}Sn$ (Mn-Pt-Pd-Sn) were grown. These ingots are polycrystalline: the individual crystalline grains are identified by electron backscattered diffraction (EBSD).[30,31] **Figure 1a** shows the EBSD of a typical sample. The various hues correspond to the orientation of the different grains. As illustrated on the right side of Figure 1a, EBSD gives a map of the inverse pole figure (IPF), in which the orientations [100], [110], and [001] are distinguished by the colors green, blue, and red, respectively. Using focused ion beam milling (FIB), thin lamellae can be cut from one of these single crystalline grains identified by EBSD. Since the DMI vector in the D_{2d} system only has non-zero components along the [100] and [010] crystallographic directions within the tetragonal basal plane of the Mn-Pt-Pd-Sn compound, lamellae are cut from the red region of the bulk sample with their surface perpendicular to the [001] direction. A transmission electron microscopy (TEM) image of one of these lamellae is displayed in Figure 1b. The black and gray contrasts in the image show that the left side of the lamella is thicker (400 nm) than its right side (170 nm). A selected area electron diffraction (SAED) pattern on the right side of the lamella, as shown in Figure 1c, confirms

**ADVANCED
SCIENCE NEWS**

www.advancedsciencenews.com

**ADVANCED
FUNCTIONAL
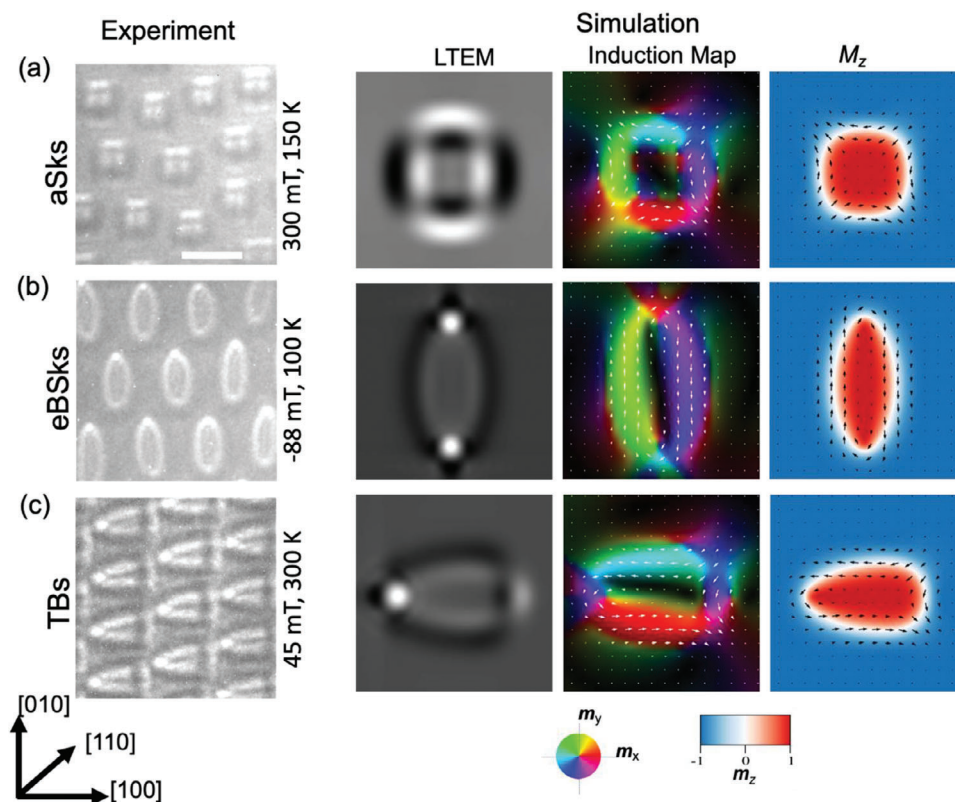MATERIALS**

www.afm-journal.de

Figure 2. Spin textures in Mn-Pt-Pd-Sn. a–c) First column shows the experimental observation of antiskyrmions (aSks), elliptical Bloch skyrmions (eBSks) and trivial bubbles (TBs) in Mn-Pt-Pd-Sn at different magnetic fields and temperatures mentioned in sides to each LTEM images. Second, third, and fourth columns show the simulated LTEM, induction map, and components of magnetization for aSk, eBSk, and TB. The color wheel highlights the angle of the magnetization and color bar highlights the z component of magnetization. The white and black arrows in induction map and M_z indicate the direction of the in-plane magnetization. The scale bar in (a) corresponds to 300 nm and same for the LTEM images in (b, c).

that the surface normal of the lamella is indeed oriented along [001]. Here we report, using Lorentz transmission electron microscopy (LTEM), real-space imaging of the magnetic contrast in two lamellae with thicknesses of 170 nm (see Figure 1b, lamella L1) and 280 nm (lamella L2), respectively. Experimental LTEM images and micromagnetically simulated spin textures of aSk, eBSk, and TB, the predominant spin textures found in the D_{2d} Heusler compound Mn-Pt-Pd-Sn, are shown in **Figure 2a–c**. The magnetic induction derived from the micromagnetic simulation, the so-called simulated LTEM textures, and the experimentally observed LTEM images agree well with each other. An aSk has a complex spin texture: Bloch walls with right-handed (RH) and left-handed (LH) chiralities are found along the [100] and [010] crystallographic directions, whereas Néel walls are found along the [110] and [1-10] crystallographic directions (Figure 2a, white and black arrows in induction map and M_z). By contrast, eBSk has only Bloch walls (Figure 2b). These aSk and eBSk are observed at zero tilt of the lamella, whose long axis of the tetragonal [001] direction coincides with the electron beam propagation direction in the normal incidence condition. Whereas, TB is mostly observed when tilting the lamella away from the zero-tilt in the presence of a magnetic field (see Figure S1, Supporting Information), which has two Néel walls directed along the [110] and [1-10] directions (Figure 2c).

The magnetic ground state in zero magnetic field of Mn-Pt-Pd-Sn is a 1D helical spin texture whose helical axis is oriented along one of two in-plane crystal directions [010] and [100] for which Bloch walls are stabilized by DMI and which have a lower magnetostatic energy as compared to Néel walls.[24] When an out-of-plane (OOP) magnetic field is applied along the [001] direction the helical state evolves directly into a saturated ferri-magnetic state without the formation of any skyrmions (Figure S2, Supporting Information). However, an in-plane magnetic field can help to stabilize skyrmions.[26] In the TEM a magnetic field can be applied by using the objective lens coils which are not otherwise used for Lorentz TEM imaging. This field, H, is parallel to the TEM column, so to realize a magnetic field with an in-plane component the lamella must be tilted (from the zero tilt angle condition, $\theta = 0°$) so that its normal is at an angle to the TEM column axis. We use a typical procedure in which the lamella is first tilted away from $\theta = 0°$ in the presence of a magnetic field, H, and then tilted back to $\theta = 0°$ without changing the field strength. An example is given in **Figure 3** in which the 170 nm thick lamella is tilted to $\theta = 40°$ toward the [110] direction and then returned to $\theta = 0°$ to record the LTEM image. Figure 3a,b shows schematics of this procedure in which the back-and-forth rotation process is indicated by purple and blue arrows, respectively. This procedure is repeated with increasing strength of the magnetic field at
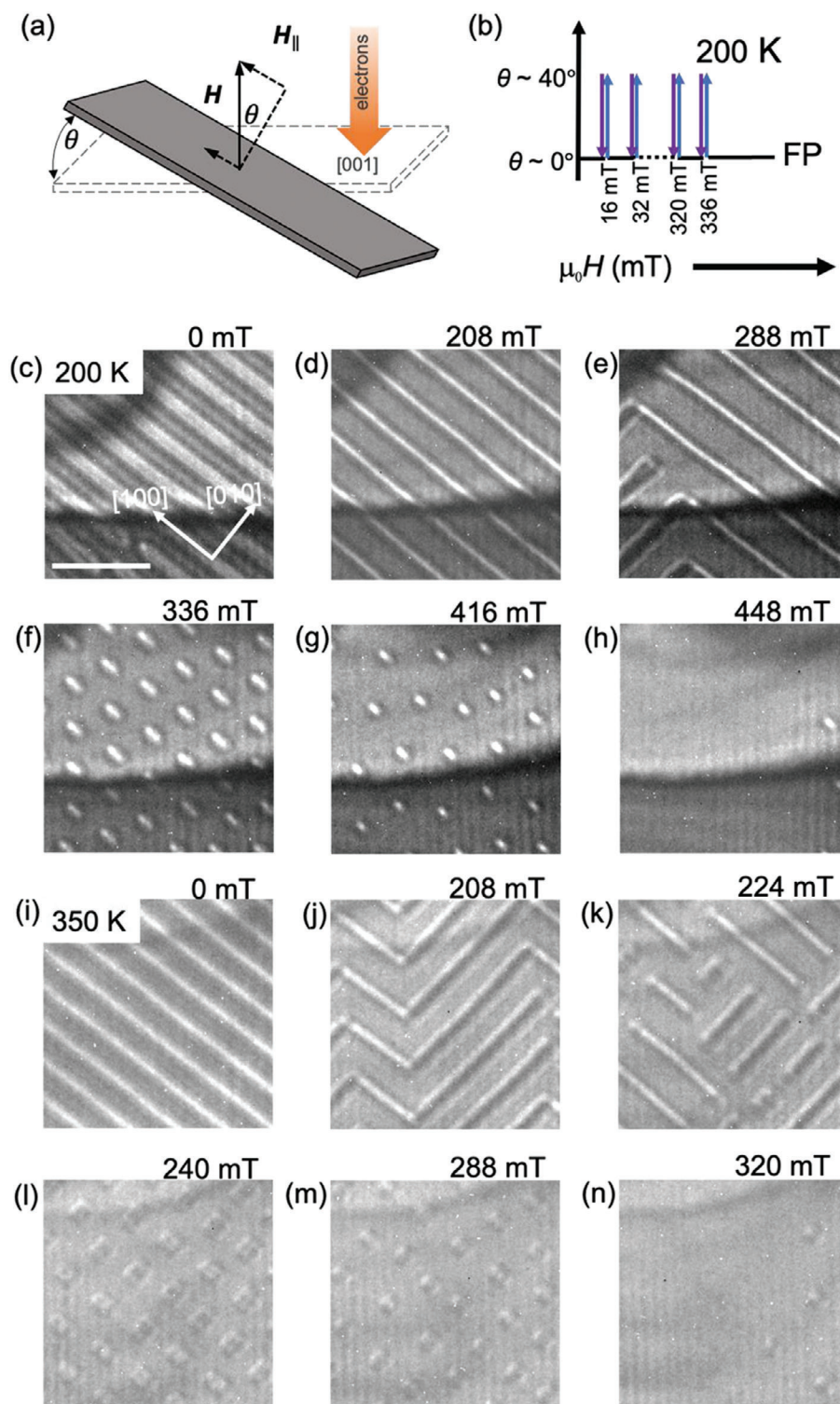
Figure 3. Evolution of spin textures from the helical state. a) Illustration of the geometry of the lamella used for the LTEM measurements in which the lamella is tilted along a given in-plane direction by an angle theta. The field H is aligned along the TEM's column perpendicular to the plane of the untilted lamella. b) Schematic of the tilting process by which the lamella is subject to a series of in-plane fields by tilting in a sequence of fields H. c–n) LTEM micrographs showing the evolution of topological spin textures at 200 K for a $\approx$170 nm thick lamella starting from the helical phase. c–e) Helical phase at 0, 208, and 288 mT, respectively. f) Lattice state is found at 336 mT. g,h) At 416 mT; the density of the nano-objects decreases. (f) Only two eBSks are left at 448 mT. i,j) Helical phase at 0, 208 mT, respectively at 350 K. k) Few aSks are formed. l) Lattice state at 240 mT. m,n) At 288 and 320 mT, the density of aSks decreases. All images are at the same scale: the scale bar in (c) corresponds to 500 nm. The crystallographic directions are indicated in (c).
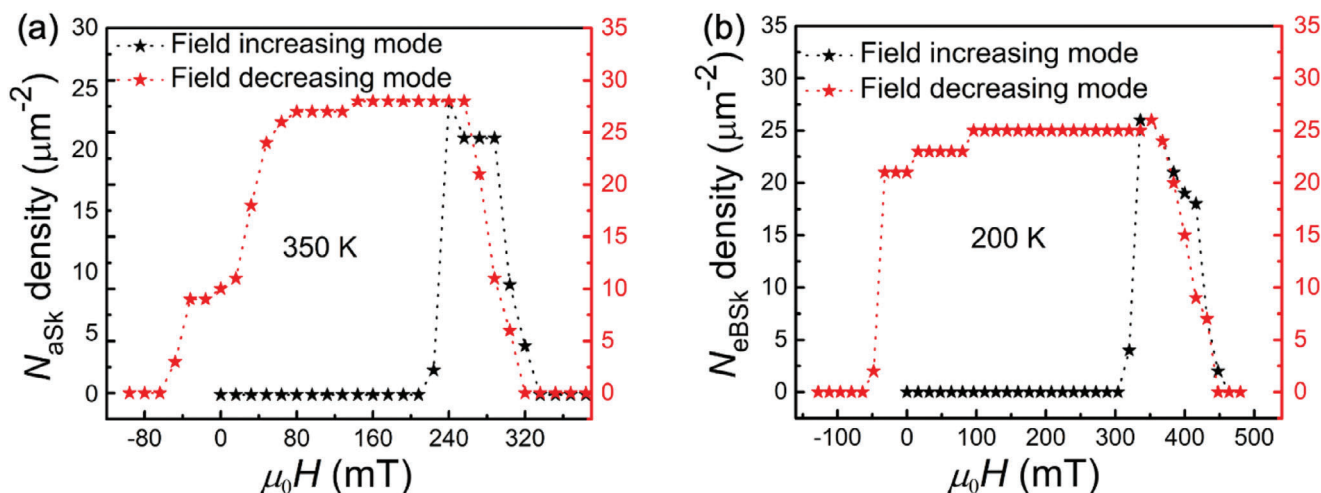
ADVANCED
SCIENCE NEWS

www.advancedsciencenews.com

ADVANCED
FUNCTIONAL
MATERIALS

www.afm-journal.de

Figure 4. Density of spin textures in field increasing and decreasing modes. The density of nano-objects for aSks and eBSks vs magnetic field at a) 200 and b) 350 K in increasing and decreasing field modes is shown as black and red curves, respectively. The data plots for increasing and decreasing field modes are obtained from a series of LTEM images at different magnetic fields and temperatures. Selected images are shown in Figure 3 (increasing field mode) and Figure S4 (Supporting Information) (decreasing field mode).

temperatures ranging from 100 to 355 K, which is the accessible temperature range in our TEM sample holder. The magnetic field at each temperature is varied from zero till the saturation state of the lamella is reached.

Now we discuss the spin textures in the 170 nm thick lamella in detail. The ground state at 200 K in 0 mT after cooling from 300 K in zero field before any tilting experiments are carried out is shown in Figure 3c. The periodicity of the helices increases with applied magnetic field as shown in Figure 3d,e and Figure S2 (Supporting Information). Note that it has earlier been shown that tilting along the [100] or [010] directions in a large enough field stabilizes helices that are directed along the [100] and [010] directions, respectively. Tilting along the intermediate [110] or [−110] directions gives helices randomly oriented along the [010] and [100] directions.[24,26] This also is the case for the data shown in Figure 3e at 288 mT. As the field is further increased (with tilting at each field step) the helical ground state evolves into an eBSk lattice state, as shown in Figure 3f at 336 mT. As the magnetic field is further increased, the density of eBSks diminishes, and their size is reduced (Figure 3g). Just two eBSks remain at 448 mT (Figure 3h) and at higher fields the lamella attains a fully saturated ferrimagnetic state. Similar observations are found at temperatures of 150, and 250 K but the field above which the eBSks are observed is higher at 150 K and lower at 250 K. The saturation field is also higher at 150 K and lower at 250 K.

It is known that Mn-Pt-Pd-Sn exhibits a spin reorientation transition below ≈133 K where the collinear ferrimagnetic state evolves into a non-collinear state because of canting of the magnetic moments on one of the Mn sublattices away from the tetragonal axis [001], the uniaxial anisotropy direction.[11,32] Below this transition only sparse states of eBSk are observed in the ≈170 nm thick lamella. The maximum tilting angle in our experimental setup is 40° which limits the maximum in-plane field that can be applied to the sample. A larger in-plane field is necessary to initiate a lattice state for this lamella since in the second much thicker lamella (≈280 nm) an eBSk lattice state can be stabilized

at 100 K (Figure S3, Supporting Information) but only by tilting the sample to the maximum possible tilt angle.

At room temperature and above, we find mostly aSks (Figure 3i–n) after tilting in increasing fields. Just as above, decreasing the magnetic field from the saturation state to zero field without tilting stabilizes the helical phase, as shown at 350 K (Figure 3i). At 350 K as the field is increased (using the tilting procedure above) a few aSks first appear at a field of 224 mT (Figure 3k) and a square lattice of these objects appears at 240 mT (Figure 3l). At 320 mT only a few isolated square aSks are observed (Figure 3n).

The stability region for topological spin textures is found to be narrower using the above procedure when the sample is first cooled in zero field from room temperature to a given temperature and then the field is increased using the tilting procedure discussed above, than when first applying a large field to reach the fully magnetized state at any studied temperature and then using a similar tilting protocol, as the field is systematically decreased.[26] Thus there is a large magnetic field hysteresis in the boundaries between the different spin textures at any given temperature. For example, the field stability window for eBSk and aSk at 200 and 350 K, respectively, is almost 3 times larger for decreasing field than for increasing field, as illustrated in **Figure** 4a,b. (Also compare Figure 3 with Figure S4, Supporting Information). Therefore, we can deduce that the transition from nano-objects to the helical phase requires a significant activation energy, resulting in a broad stability window for these nano-objects.[33] Nonetheless, in all cases, the helical phase appears from the aSk or elliptical Bloch skyrmion lattice states when the magnetic field is lowered to zero or negative field values, causing the nano-objects to collapse, as explained in the following section.

In the following, we investigate how the magnetic field affects the arrangement of the different spin textures that are organized in lattices. Here we use our Lamella L1 although the results are, in general, similar for both lamellae (See Figure S5, Supporting Information for Lamella L2). For this purpose, we consider first
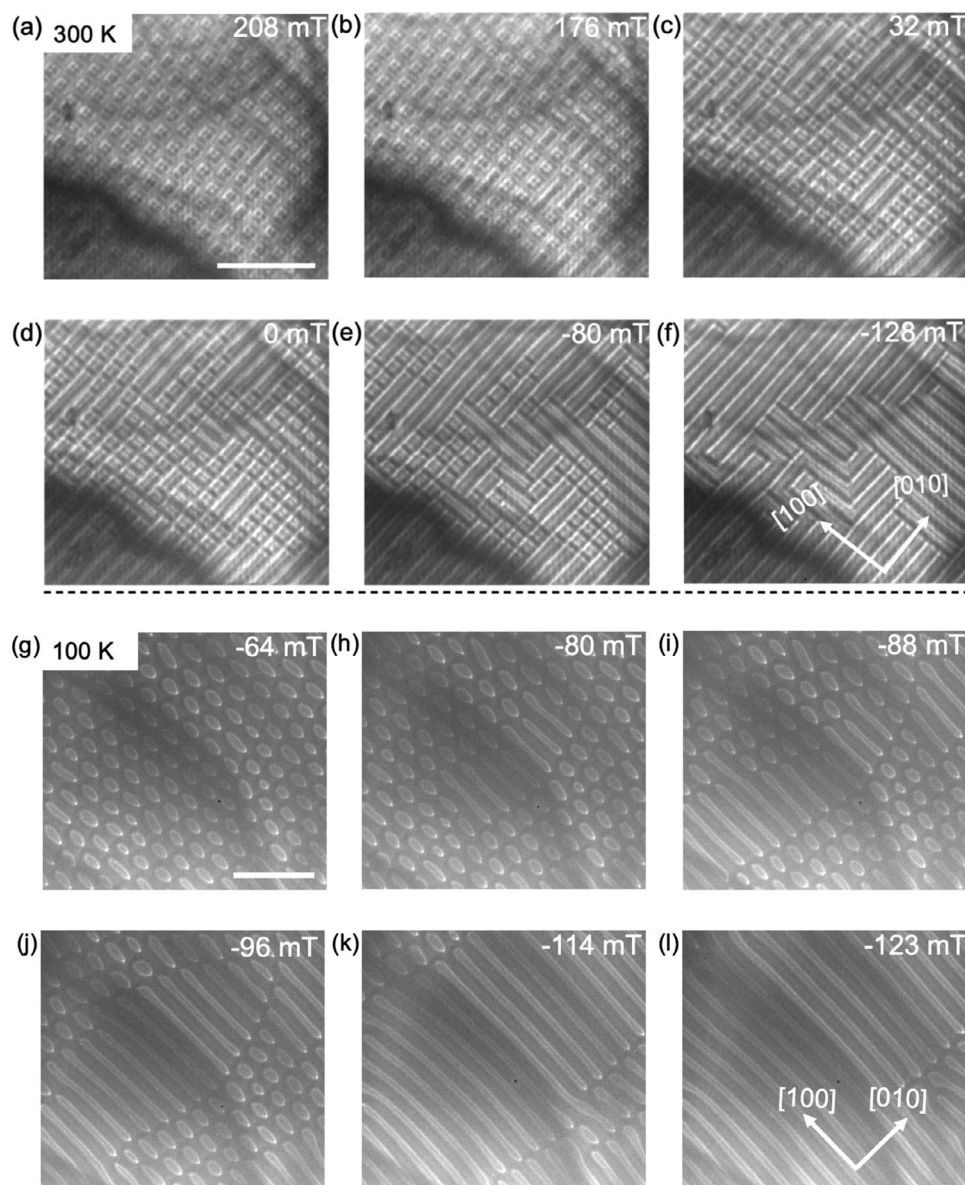
Figure 5. Collapse dynamics of aSks and eBSks. a–f) Decreasing the field from an aSks lattice and their collapse into short helices for Lamella L1. For Lamella L2, see Figure S5 (Supporting Information). The short helices are rectangular in shape. c–e) By joining short rectangular helices with the other square aSks (in negative field directions), more short helices are formed. In (f), no square aSks are found. The short helices are elongated along the [100] or [010] directions. The scale bar in b–f is the same as in (a), which is 1 µm. g) Lattices of eBSks found at 208 mT in Lamella L2. h) Elliptical skyrmions (in the middle) join together to form elongated elliptical shapes. i,j) More short helices in elliptical shape are found on joining the eBSks. k) At −114 mT only a few eBSks are left in the corner of the LTEM image, and short helices are further elongated. l) Helical phase is formed. The scale bar in h–l) is the same as in (g), which is 1 µm.

the lattice of aSks illustrated in **Figure 5**. Figure 5a shows a close-packed aSk lattice state at 300 K in a field of 208 mT formed using the aforementioned field-decreasing protocol from the saturation state at ≈396 mT. The aSk state appears initially at a field of 304 mT and is essentially unchanged as this field is reduced to 208 mT. However, when the field is further reduced, some of the square-shaped aSks become elongated, as shown in Figure 5b for a field of 176 mT. Since the state is close-packed the elongation of one aSk leads to the contraction of nearby aSks. As the field is further reduced short helices are formed as an aSk is elongated and

then such elongated aSks join together (Figure 5c–e). Figure 5c depicts a state with square aSks and few short helices. As the field is reduced to zero and a negative field is applied, larger numbers of square aSks combine to form greater numbers of short helices. The remaining square aSks combine with previously observed short helices to form longer helices (Figure 5b–e). At −80 mT (Figure 5e), there are only a few square aSks at the connections between short helices of varying lengths. In Figure 5f, there are no aSk objects with a square shape and the region is filled with the helical state.

ADVANCED
SCIENCE NEWS

www.advancedsciencenews.com

ADVANCED
FUNCTIONAL
MATERIALS

www.afm-journal.de

We used the similar protocol for forming the eBSk lattice at 100 K as we did for the aSk lattice at 300 K. At this temperature of 100 K, the eBSk lattice appears at 400 mT, and the lattice remains stable up to a negative field of -64 mT (Figure 5g). In this sample as well as the 170 nm thick sample, we observe predominantly eBSks that have their long axis oriented along the [100] direction and none along the perpendicular direction. There is an exception to some data from the 170 nm-thick sample at 150 K, where eBSks were found along the [010] direction in a micron-sized region, as shown in ref. [26] Because of the clockwise and counter-clock-wise rotation of the magnetizations, the eBSks with long axes oriented along the [100] direction have a white Lorentz TEM contrast, whereas those with long axes oriented along the [010] direction have a grey Lorentz TEM contrast (Figure S6, Supporting Information). As mentioned above this means that all the observed eBSks in Lamella L2 have the same chirality. This broken symmetry could be due to a small strain in our sample perhaps derived from the FIB processing to fabricate the sample. We also find that as the eBSks are elongated by reducing the field to form helical-like structures, this elongation also takes place only one direction (i.e. [100]). This elongation only starts when the field is decreased through zero field to negative fields beyond -64 mT until which field there is no elongation (see Figure 5g). At -80 mT some elongated eBSks are seen which become longer and longer as the magnitude of the fields is systematically increased in the negative direction eventually reaching more than 2 μm in length (Figure 5h–k; Figure S7, Supporting Information). Real-space imaging in the LTEM shows that these are formed by the combination of neighboring eBSks. Both ends of the helices, whether short or long, are similar in shape to those of the eBSks. (Similarly, the ends of the helices formed from combining the aSks in Figure 5b–e has the same shape as the aSk). These elongated objects have the same topological charge as the eBSks ($N_{SK} = -1$) or aSks ($N_{SK} = +1$). Each end of each of the short helices has $N_{SK} = -\frac{1}{2}$ (for an elongated eBSk) or $+\frac{1}{2}$ (for an elongated aSk), and the contribution from the center area is zero. A similar evolution of the skyrmions has been found from micromagnetic simulations and the terminal regions of the elongated skyrmions are described as being a meron (see Ref. [34]). At −123 mT (Figure 5l), when the helices touch the boundary of the lamella (not shown here), a complete helical phase is formed, destroying the topological protection of the elongated structure. For the case of the aSk collapsing process, the topological protection was destroyed not only near the boundary of the lamella but also in the interior due to the randomly oriented short helices along the crystallographic [010] and [100] directions (Figure 5f). These elongated objects are promising candidates for applications in spin-torque nano-oscillators and magnon waveguides according to a recent theoretical proposal.[35] They are also predicted to host Majorana-bound states when interfaced with a superconductor that is potentially useful for quantum computing.[36]

Those collapse mechanisms are in stark contrast to the dynamics of B20 compounds in which Block skyrmions are observed which evolve from a cycloidal state that can be oriented along any crystal direction. In these compounds, a reduction in the applied field first induces a non-equilibrium phase separation into regions of skyrmions and regions of a conical structure in which the cone propagation vector is along the applied mag-

netic field.[37] Near zero field, this conical phase evolves into a helical phase with a propagation vector perpendicular to the applied magnetic field. In our Mn-Pt-Pd-Sn system a strong uniaxial anisotropy and a tubular, non-twisted, spin structure due to the anisotropic DMI exclude such a conical spin arrangement. Therefore, the extensive length deformation of our spin textures and their collapse dynamics from a dense lattice state have not yet been explored. Since the elongations of the eBSks and aSks along the [100] and [010] directions coincide with the material's components of the intrinsic DMI vector, it appears that the elongation is predominantly determined by the system's intrinsic DMI.[38] To further elaborate on this effect, we have provided an additional micromagnetic simulation that confirms that aSk can elongate along the Bloch wall directions either when the strength of the DMI or magnetic field varies in the presence of dipolar interactions (Figure S8, Supporting Information). Skyrmions can also become elongated and take irregular shapes due to mechanisms such as spin-orbit torque (SOT) or spin-transfer torque (STT)[39–42] or because of constricted geometries such as nanostripes.[28,43]

We have corroborated the field-driven transformation of spin textures that we discussed above by carrying out micromagnetic simulations using the open-source GPU-accelerated Python library magnum.np[44] and starting from a parametrized lattice state of eBSks (aSks) using an effective temperature $T_{eff} = 100$ K ($T_{eff} = 300$ K) at an OOP magnetic field of 500 mT (450 mT). Note that the temperature is introduced indirectly, by using temperature-dependent effective magnetic parameters. We solve numerically the Landau-Lifshitz-Gilbert (LLG) equation taking into consideration energy contributions from demagnetization, exchange, anisotropy, DMI, and Zeeman fields; see Experimental Section for more details. These numerical investigations reveal that aSks, depicted in their isolated magnetization state in **Figure 6a,b**, as well as the elongated bar states, are metastable, as illustrated in Figure 6c,d. When the field is lowered the aSks first elongate and ultimately join together into longer helices, as observed in Figure 6e,f. In Figure S9 (Supporting Information) we show the topological charge density of these elongated eBSks and aSks. Note that in our simulations the lattice state is not as closed-packed as in the experiments. Thus, it does not allow us to exactly reproduce the adjacent joining of square aSks observed in the experiments. A further reason for the discrepancy of the field-driven collapse mechanism is that the topologically protected aSks will have a finite energy barrier to merging, which might be overcome by temperature fluctuation in the experiments. A similar field-driven mechanism is observed if one starts from a lattice state of eBSks. The exemplary magnetization state of an isolated eBSk is shown in Figure 6g,h. In the performed magnetic simulations few eBSks are already very elongated in our simulations, as shown in Figure 6i,j. The eBSks elongate even more into helices when the field magnitude is lowered, ultimately joining together as in the experiments Figure 6k,l. However, the helices are joined only at the surfaces, as we depicted in Figure 6. In the bulk region, the same behavior as for aSks appears, where the micromagnetic simulations without thermal fluctuations are not able to resolve the merging of Bloch points and the resulting dynamics.

Apart from aSks and eBSks, TBs are also seen experimentally in Mn-Pt-Pd-Sn. TBs have one half that is Bloch type and the other half has a structure akin to aSks, so that thereby $N_{SK} = 0$.

ADVANCED
SCIENCE NEWS

www.advancedsciencenews.com
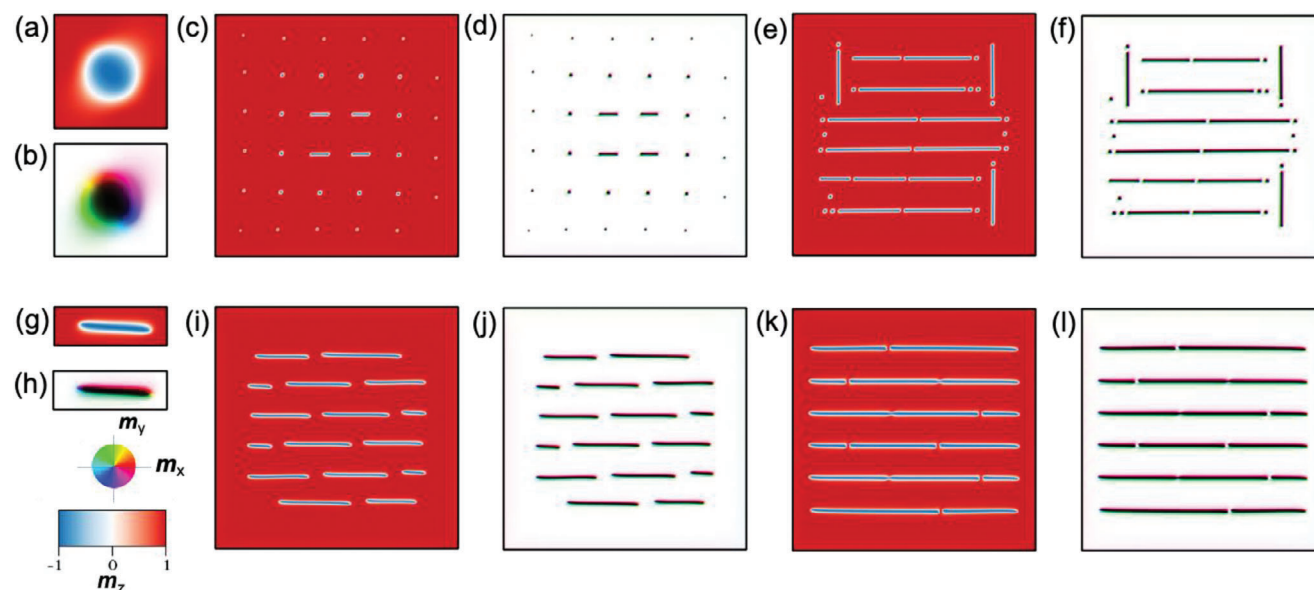
ADVANCED
FUNCTIONAL
MATERIALS

www.afm-journal.de

Figure 6. Micromagnetic simulations to describe the field-driven collapse mechanism. An aSk a,b) is shown in two color schemes, where the first highlights the z component of magnetization, whereas the latter highlights the angle of the magnetization rotation given by the color wheel. A lattice with aSks at $T_{eff} = 350$ K and an OOP field of 450 mT is illustrated in c), and d) in the two color schemes, respectively. After the magnetic field is decreased to 341 mT the aSks are joined and become elongated along both the [100] and [010] directions, as shown in e,f). In the case of eBSks illustrated in g,h) the lattice of already elongated spin-objects from i,j) collapses into stripe domains of the same chirality in k,l) if one simulates the system at $T_{eff} = 100$ K and a magnetic field decreasing from 500 to 340 mT. A few of the elongated objects in k,l) have Bloch-type walls at one end and aSks-type walls at the other end, resulting in elongated TBs (also see Figure S9d, Supporting Information).
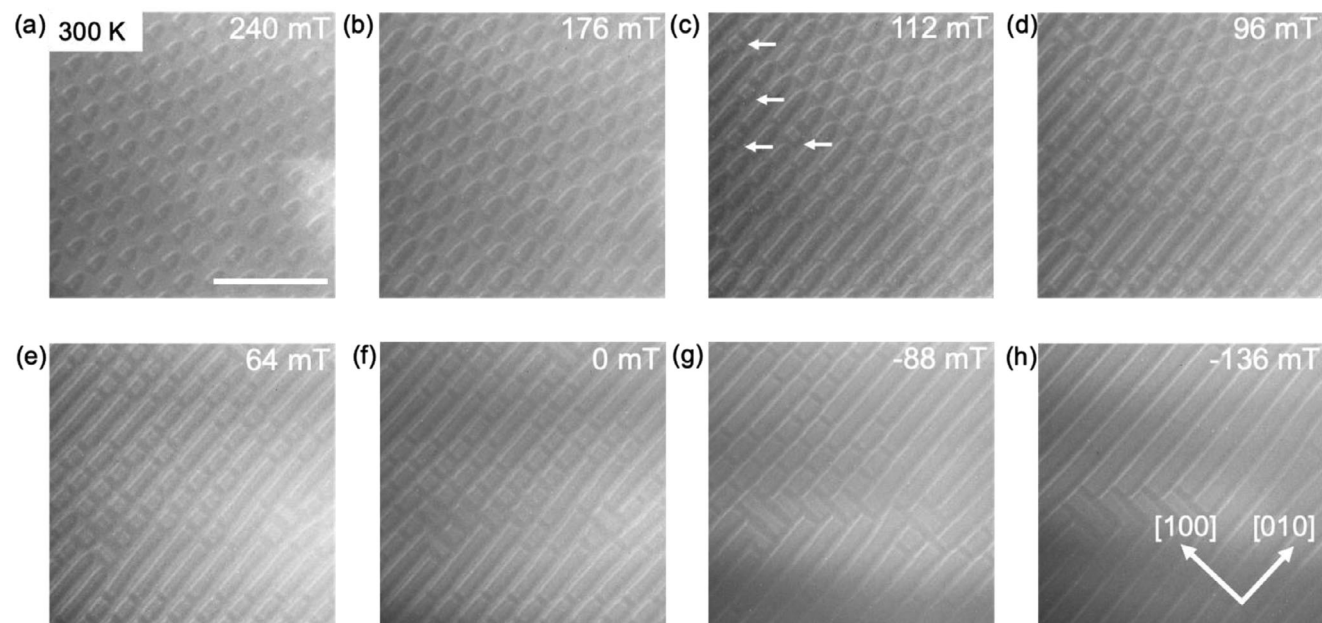

Figure 7. Collapse dynamics of TBs. a–h) The LTEM are imaged ≈14° away from the [001] axis and out-of-field values are mentioned at the top corner of each LTEM image. a) A TB (type-II) lattice state is shown at $H = 240$ mT. (b) Reducing the magnetic field, these TBs are elongated. c) At 112 mT a few trivial objects connect with each other and four aSks are formed (marked in white arrows). d) Lowering H a greater number of aSks and elongated aSks are formed. e,f) At 64 and 0 mT, the region is filled with aSks and elongated aSks. g) The density of square aSks decreases by forming a helical phase. h) A helical phase is formed at −136 mT. The scale bar in (b-h) is the same as in (a), which is 1 µm.

ADVANCED
SCIENCE NEWS

www.advancedsciencenews.com

ADVANCED
FUNCTIONAL
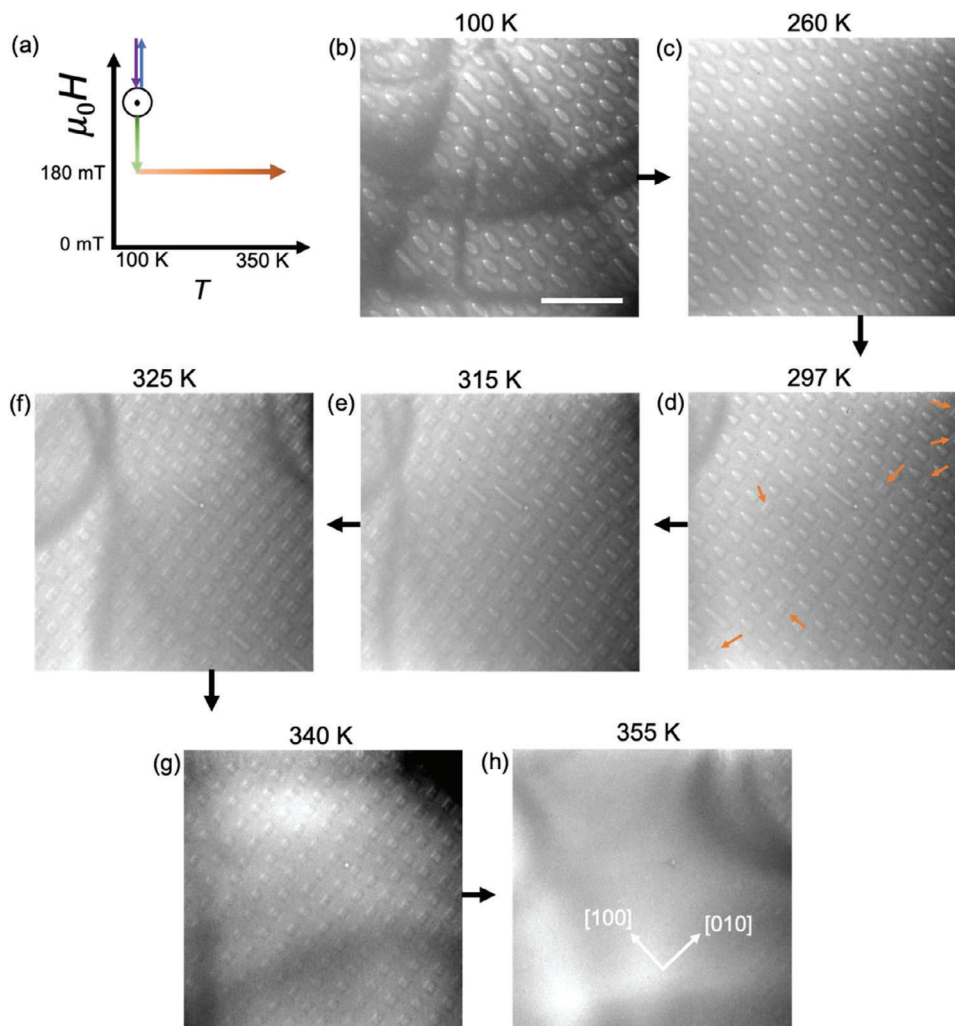**MATERIALS**

www.afm-journal.de

Figure 8. Heating experiment from an eBSks lattice state. a) Schematic diagram of the heating experiment. b) An eBSk lattice state is formed at 100 K and zero tilt after a temporary in-plane field application at a high magnetic field of $H = 368$ mT. H is then reduced to 180 mT. c–h) The temperature is increased to 355 K while keeping H constant. Different states are obtained as follows: d,e) TBs and aSks, f,g) aSks lattice and h) sparse state. Orange arrows in (d) point to aSks. The scale bar in (b) corresponds to 1 μm and same for all the LTEM images.

These objects are created under certain tilting and field conditions, namely a tilt of a few degrees away from the [001] direction for certain fields (see Figure S1, Supporting Information). First, we created the antiskyrmion lattice using the same method we used to get Figure 5a. The magnetic field was then lowered to 240 mT at zero tilt, and a TB state was found by tilting the sample to $\theta = 14°$ at 300 K, as shown in **Figure 7a**. To investigate the mechanism of TB collapse, the magnetic field was lowered while keeping the lamella at $\theta = 14°$. Initially, only a few of the TBs become elongated on joining with each other, as shown in Figure 7b–d. Intriguingly, however, we did not observe a prominent melting process among TBs but rather saw these nano-objects start to transform into aSks or elongated aSks (Figure 7c,d). The collapsing process produces more elongated aSks via joining with other aSks or with elongated aSks when the field is reduced further (see Figure 7f,g). Finally, a helical state is formed at −136 mT (Figure 7h). The transformation from TBs to aSks in this experiment suggests that aSk is more robustly

metastable than TB at room temperature and low field. In Figure S10 (Supporting Information), we plotted the number of objects vs. magnetic field, demonstrating how the density of aSks, eBSks, and TBs decreases with decreasing magnetic field.

Besides the field-dependent stability and collapse dynamics of the spin-textures, their thermal stability plays a key role in their integration into spintronic devices. Hence, we investigated the resilience of various spin textures to heating and cooling. First, we will discuss the experimental investigation into the stability of eBSks against heating in a constant magnetic field. We wish to see whether these eBSks persist at higher temperatures than the typical stability region for eBSks (below room temperature) or whether a phase transformation to an aSk state takes place. With the help of the similar protocol shown in Figure 5, the triangular lattice of eBSks is first stabilized at 398 mT and at a temperature of 100 K. The out-of-plane field was subsequently lowered to 180 mT. **Figure 8a** shows the schematic diagram of the subsequent heating experiment. Figure 8b presents the LTEM contrast

**ADVANCED
SCIENCE NEWS**

www.advancedsciencenews.com

**ADVANCED
FUNCTIONAL
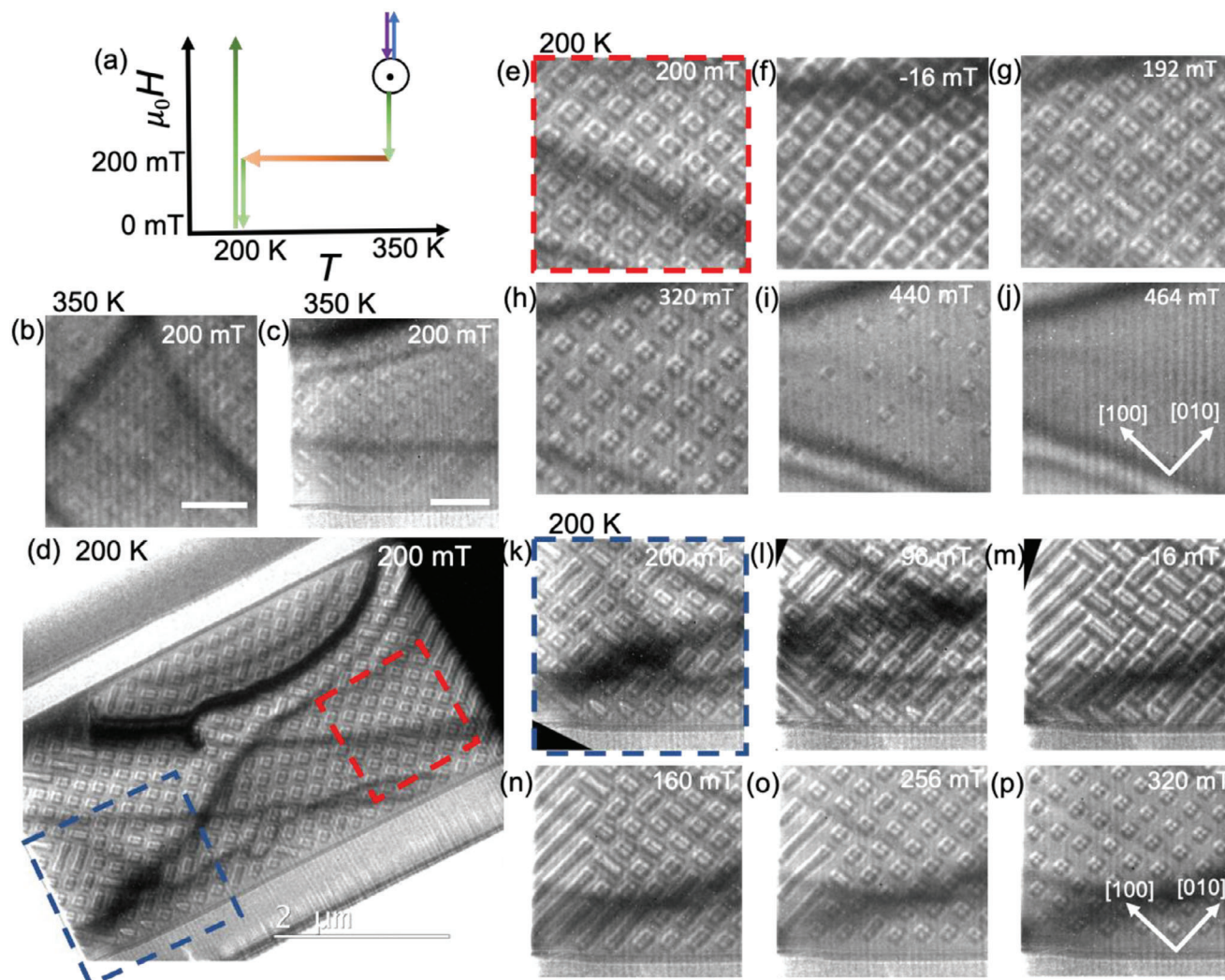MATERIALS**

www.afm-journal.de

Figure 9. Magnetic aSks formed using a field-cooling procedure: a) Schematic diagram for the field-cooling procedure. b,c) An aSk lattice at 350 K and 200 mT. The LTEM images are taken from two different regions of an extended lamella. The scale bars in a,b) correspond to 400, and 500 nm, respectively. d) The lamella is cooled down to 200 K keeping H constant. LTEM image of the full lamella at 200 K after thermalization to ensure stability. e–j) LTEM contrasts at different magnetic fields from the region marked by the red rectangle in (d). First, the field is reduced to −16 from 200 mT and then the field is increased to 464 mT. The scale bar in e–j) is the same as in (a). k–p) LTEM images at different magnetic fields from the region marked by the blue rectangle in (d). In (n) at 160 mT, the three TBs and one aSk in the bottom region of k–m) are changed to elongated objects with an elongation direction along [010]. At higher magnetic fields, square aSks are formed. The scale bar in k–p) is the same as in (b). Please note that (b, c) regions are the same region as marked by in (d) but at 350 K.

of the eBSks recorded at 100 K and 180 mT. A small portion of the entire lamella is shown here and in Figure S11 (Supporting Information), we presented the LTEM contrast of the full lamella. We increased the lamella's temperature to 355 K while keeping the magnetic field constant (180 mT). Up to 260 K, these eBSks are quite stable (Figure 8c). At 297 K (Figure 8d) these eBSks became deformed. The nano-objects of distorted shape reflect a structure of a TB with zero topological charge which are extended along the [100] crystallographic direction. At this temperature, we also observed the formation of very few square-shaped aSks. Those objects are indicated by orange arrows in Figure 8d. With an increase in temperature by 18 K (Figure 8e), a considerable number of aSks are found alongside a few TBs. Moreover, at 325 K, TBs transform to aSks (Figure 8f). At 315 K a few small helices are

found. Additionally, as illustrated at 297 and 315 K, some short helices were also generated. A few short helices were also observed at 315 K, and even fewer at 325 K. At 340 K the lamella contains only aSks (Figure 8g). Here, the size of the aSks is diminished by compressing the domains. As the temperature is increased further, the aSks begin to annihilate. As illustrated in Figure 8h, there are only a few aSks remaining at 355 K, and the region is mostly in a polarized state.

Our experiments give important insights into the behavior of the spin textures in Mn-Pt-Pd-Sn. The eBSks, stabilized by a dominant DDI, are observed over a broader temperature range in contrast to the aSks. Consequently, when the Heusler compound is heated above 300 K, the transformation of eBSks to aSks suggests that the DMI becomes the dominant interaction,

**ADVANCED
SCIENCE NEWS**

www.advancedsciencenews.com

**ADVANCED
FUNCTIONAL
MATERIALS**

www.afm-journal.de

while the relevance of DDI decreases at higher temperatures, as the magnetization is lowered. It is important to note that similar experiments have been conducted on another related compound Mn-Rh-Ir-Sn, which also possesses the D_{2d} crystal symmetry. However, no topological phase transition similar to that observed in Mn-Pt-Pd-Sn was found.[45] This discrepancy can be attributed to the reduced DMI and lower spin-orbit coupling resulting from the 4d element Rh in Mn-Rh-Ir-Sn in contrast to the 5d element Pt in Mn-Pt-Pd-Sn. It's also worth mentioning that for Mn-Pt-Pd-Sn, in the temperature induced process, in which eBSks are transformed into TBs and aSks, the eBSks are primarily observed in a triangular lattice state, whereas the aSks are found either in a triangular lattice or a square lattice state, depending on the temperature. A detailed analysis is given in Figure S12 (Supporting Information).

Lastly, we used a field-cooled protocol to find out how stable aSks are at different temperatures by cooling the lamella filled with aSks from 350 K down to various low temperatures. The schematic in **Figure 9a** illustrates the cooling procedure that was used. First, the aSk lattice state was created at 350 K in a field of 232 mT using the similar stabilization procedure discussed above in Figure 5, following which the field was then reduced to 200 mT. Figure 9b,c highlights two different regions of the LTEM image of the lamella at 350 K. The lamella was then cooled down to 200 K under the same constant magnetic field (200 mT). Figure 9d depicts the LTEM contrast of the entire lamella after ensuring the thermal stability of the spin texture by waiting for 30 min at 200 K. Two regions, denoted by the red and blue squares, are the regions depicted in Figure 9b,c. First, we discuss the region depicted by the red square in Figure 9d as the field is varied. This region displays a short helix (rectangular in shape) within a lattice of aSks. When the magnetic field is reduced to −16 mT (Figure 9f) the metastable aSks are still found. Then, LTEM images were collected as the field was increased in steps of 16 mT. At ≈256 mT the lattice is still square (Figure 9g) and the short helix has transformed into a square-shaped object (Figure 9h). As the magnetic field is further increased the aSk lattice first becomes partially disordered, and, finally, fully disordered at higher fields. An isolated state of aSks is found in even stronger magnetic fields (Figure 9i) before the lamella becomes fully polarized (Figure 9j).

Now we discuss the region highlighted by the blue square in Figure 9k. A mixture of aSks and rectangular short helices is seen within this region. When the field strength is decreased, the aSks tend to become longer while more short helices are generated, as shown in Figure 9l,m. Conversely, increasing the magnetic field strength causes the short helices to convert into square aSks, resulting in a lattice state (see Figure 9n–p). This process demonstrates the reversible transformation of field-cooled aSks to short helices and back to aSks. The field-cooled protocol described in Figure 9a was repeated at temperatures of 100 and 250 K. Notably, unlike the field-heating experiment, we did not find that the aSks transformed to eBSks. The metastable aSks, however, were very stable at any given field and temperature for up to 4 h, the maximum time that the sample holder could maintain the temperature. This shows that the aSks in D_{2d} system have a long lifetime, as proposed.[33,46]

To observe the stabilization of square aSks in the increasing field mode at room temperature and above, we employed a stepwise procedure. Initially, the aSks were stabilized at a higher
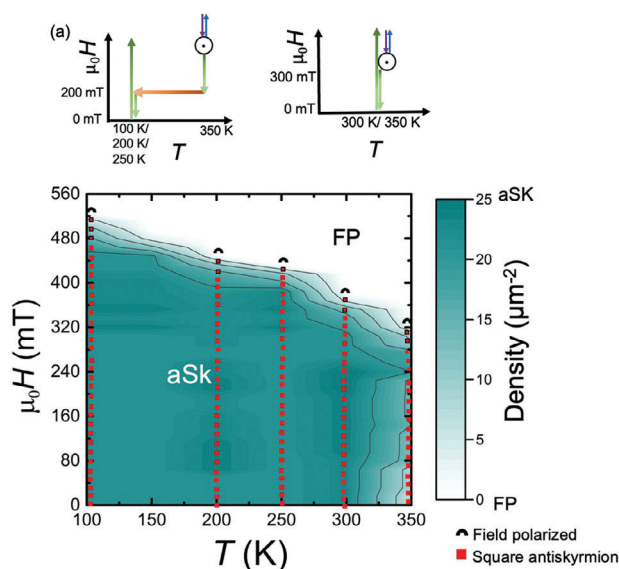

Figure 10. Magnetic phase diagram for aSks stability. a) Magnetic phase diagram which shows square aSks throughout the temperature and field in increasing mode of the magnetic field. The schematics on the top of the phase diagram show the field-cooled protocols for 100, 200, and 250 K (left side) and 300, and 350 K (right side), respectively.

field, followed by a reduction of the magnetic field to zero. Subsequently, we gradually increased the magnetic field while ensuring that the lamella remains in the zero-tilt position. The upper panel of **Figure 10** illustrates the schematics of the protocols that were used at 100, 200, and 250 K on the one hand (left) and 300 and 350 K on the other hand (right) allowing us to capture LTEM images of square aSks at various temperatures in the increasing field mode. The resulting formation of square aSks over a wide range of fields and temperatures is presented as a contour plot in Figure 10.

We now consider the stability of the nano-objects using micromagnetic simulations, where we initialize our simulations with either an eBSk, a TB, or an aSK. The magnetization state is distorted randomly, i.e. we add to each cell a random vector with a constant length and then renormalize the magnetization. This distortion is applied to ensure that the magnetization state does not get pinned in a local minimum and that the obtained relaxed magnetization state is indeed the true metastable state. We calculate the topological number of the final magnetization state, which is then given as a color in the phase diagrams illustrated in **Figure 11**. The dynamic transformation between the spin objects could not be observed, as the micromagnetic theory is not very well suited to describe magnetization dynamics that include Bloch singularities. Thus, we need to look at this problem from a static energetic point of view.

Figure 11a illustrates the stability range of eBSks as the effective temperature and the strength of DMI are varied in the micromagnetic simulations. The skyrmion is a metastable solution for each set of D_{2d} and T_{eff} if it does not disappear after being subject to random distortions, and finds its way back to the energy minimum. At 100 and 200 K we see that eBSks are stable solutions. Similarly, the TBs are stable around the same temperatures, as shown in Figure 11b. However, at 300 K both eBSks and TBs are
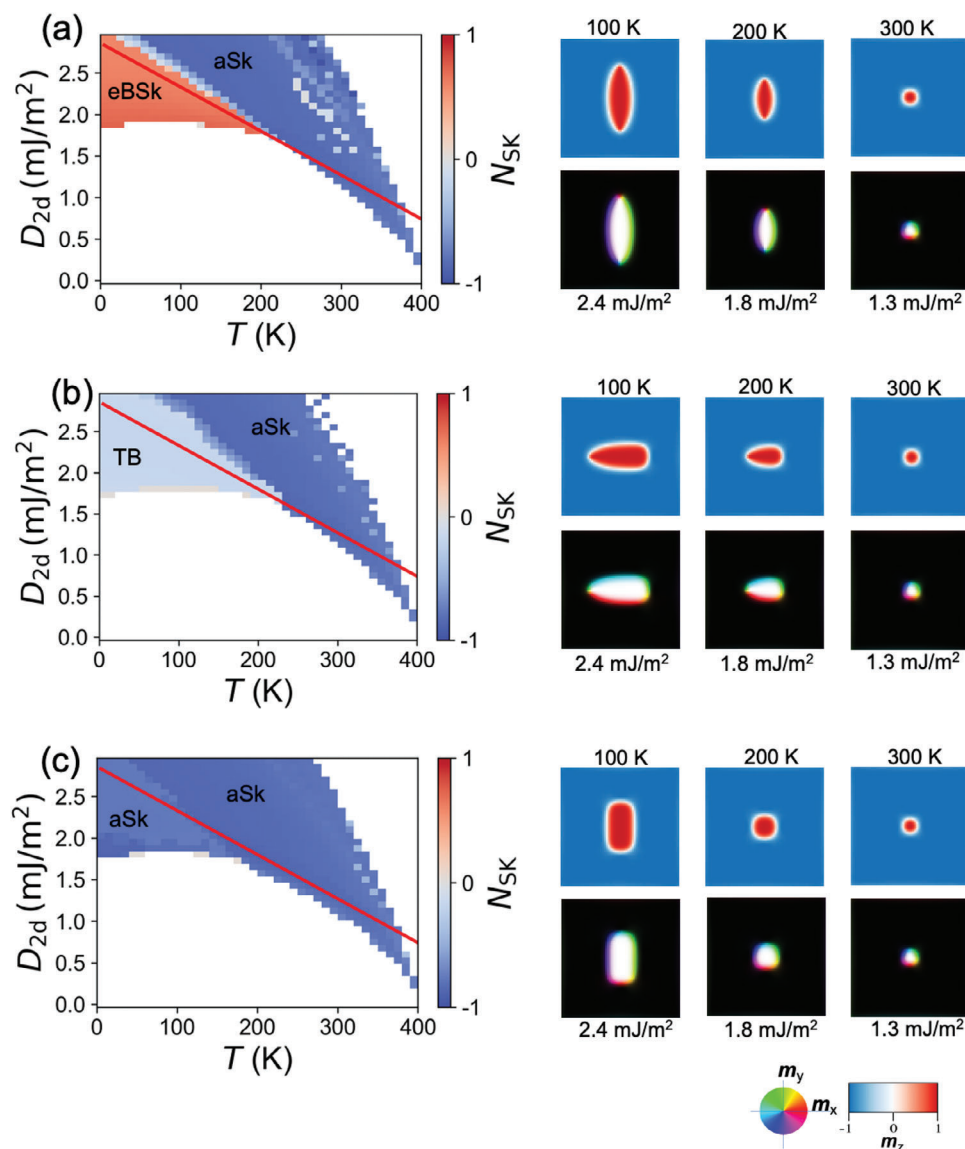
**ADVANCED
SCIENCE NEWS**

www.advancedsciencenews.com

**ADVANCED
FUNCTIONAL
MATERIALS**

www.afm-journal.de

Figure 11. Micromagnetic simulations for the temperature-dependent metastability of aSKs, eBSks, and TBs. Phase diagrams illustrating the stability regions for a) eBSks, b) TBs, and c) aSKs where the right panels illustrate snapshots of the magnetization states obtained from simulations at different effective temperatures and DMIs, along the red lines from a–c). Snapshots were taken at the center of the simulation box with a total thickness of 280 nm. The applied OOP field is 180 mT. The color wheel highlights the angle of the magnetization and color bar highlights the z component of magnetization.

no longer energetically stable solutions, and they transform into aSks. Figure 11c depicts the stability region of the aSks which has the largest stability range as compared to eBSks and TBs and are stable over the entire effective temperature range (see Experimental Section). Hence, one concludes that increasing the temperature in the experiments changes the material parameters of the system, and reshapes the energy landscape in such a fashion that eBSks are less favorable from an energetic point of view. Thus, they first become TBs, and then decay into aSks at higher temperatures. Since the aSks are stable solutions at lower temperatures as well, they do not get transformed back to eBSks. Hence, this transformation process is irreversible.

Additionally, we performed string method simulations[47–49] to investigate the temperature-dependent transformation of an

eBSk into an aSk (see Experimental Section). The resulting minimum energy paths, and the corresponding magnetization states, show that the transition mechanism is a double-occurring procedure: local transition of a Bloch wall into a Néel wall. The skyrmion decays into a triangular TB with the first transformation. The latter converts into an aSk following the second Bloch-Néel wall transition (see Figure S13, Supporting Information for snapshots of magnetizations during the collapse dynamics). Note that the energy barrier is reduced with increasing effective temperature, indicating that the thermal energy in our experiments might be sufficient to trigger the collapse dynamics. Heusler materials, that are particularly interesting for magnonic applications due to their low damping,[50,51] can, with their inherent eBSk, aSk, and TB lattices, function as natural magnonic

ADVANCED
SCIENCE NEWS

www.advancedsciencenews.com

ADVANCED
FUNCTIONAL
MATERIALS

www.afm-journal.de

crystals.[52] The field- or heat-assisted topological transformations demonstrated in our work provide the framework for reconfigurable magnonic crystals, in which frequency combs can be envisioned filtering different frequencies depending on the type of spin structures present in the system.

3. Conclusion

In conclusion, we have shown the critical role of the magnetic field, temperature, and the detailed field-temperature history protocols in the generation and stabilization, annihilation, collapse, and transformation of antiskyrmions and elliptical Bloch skyrmions in an archetypal D_{2d} Heusler compound. At all temperatures explored (100–350 K) there is a narrower field stability regime for the formation of nano-objects as the magnetic field is increased from a ground state helical phase, as compared to the case where the magnetic field is decreased from the uniformly polarized state at high fields. Our experimental findings unveiled two significant processes. First, a topological phase transformation occurs from elliptical Bloch skyrmions to antiskyrmions via the formation of trivial bubbles using a simple field-heating approach. Micromagnetic investigations revealed that it is the change in the temperature-dependent material parameters that stabilizes distinct spin textures at various temperatures. Second, a collapse mechanism leads to the formation of highly elongated spin textures. Importantly, dipolar interactions help in the elongation of the spin objects and DMI dictates the directions along which the spin textures elongate. Therefore, elongated magnetic structures exhibit a direct correlation with dipolar interactions and the D_{2d} DMI vector components along the [100] and [010] crystallographic directions. The observed prolonged elongation and metastability of magnetic textures in our work has significant implications for skyrmion-based devices and their dynamics and, hence, have to be thoroughly characterized and taken into careful consideration when developing prospective spintronic and magnonic devices. Moreover, we can envision a reconfigurable reservoir computing device where one uses skyrmion lattices as skyrmion fabrics at low temperatures but can be switched to an antiskyrmion reservoir purely by heating, enhancing the nonlinearity and versatility of the reservoir.[53–55] Our results provide invaluable insights into the intricate interplay between a system's properties and its spin textures and, thereby advance potential applications in devices.

4. Experimental Section

The bulk polycrystalline Heusler compound Mn-Pt-Pd-Sn was prepared by an arc melting method, as described elsewhere.[11] The surface of the bulk sample was smoothed by mechanical and chemical polishing procedures. Since the polycrystalline compound had different grains, the EBSD technique was carried out in a TESCAN GAIA 3 (Quantax, Bruker) system to find [001]-oriented grains. The resolution of EBSD was ≈20 nm. The electron from the scanning electron microscope (SEM) column had an accelerating voltage of 20 kV. Using a Ga$^+$ ion-based dual beam focused ion beam system [FEI Nova Nanolab 600 SEM/FIB] operated at an accelerating voltage of 2–30 kV, single crystalline lamellae with parallel surfaces were produced from the [001] oriented grain. The procedure for preparing lamellae was detailed.[26] The SEM was used to measure the thickness of the lamellae under a zero-tilt stage condition.

The SAED and LTEM measurements were performed in an aberration-corrected high-resolution transmission electron microscope [FEI TITAN 800-300]. A 60 µm selected area aperture was used to capture the diffraction pattern of the single crystalline lamella. Magnetic contrasts were acquired in Lorentz TEM mode where the magnetic field was varied from −0.28 to 2.3 T along the microscope axis by partially exciting the objective lens. The LTEM contrasts were captured from the two lamellae of different thicknesses of ≈170 and ≈280 nm used.[26] The magnetic field values were calibrated by a Hall bar sensor. The double-tilt liquid nitrogen holder was used to alter the lamella's temperature, and a temperature controller was used to maintain the temperature of the lamella at varied levels. In field-heated and field-cooled experiments, the increase or decrease of the lamella's temperature was performed at a rate of 3 K min^{-1}. The temporary tilting ≈36° toward [110] was enough to generate the aSk/eBSk lattice at zero tilt for the temperature above the spin reorientation transition temperature. However, it was observed that below the spin reorientation transition, it was needed to tilt ≈40° to get a lattice state in a 280 nm-thick sample. Therefore, to keep the tilting angle consistent throughout the whole experiment, 40^0 was given, the maximum possible tilting angle, for two lamellae, L1 and L2. The under-focus value for the LTEM imaging is ≈0.8–0.9 mm. The detailed information about the protocols used in the manuscript is provided in Figure S14 (Supporting Information).

Micromagnetic Simulations: The micromagnetic simulations that were carried out need to be classified into two categories: static relaxation and string method simulations. For all simulations the D_{2d} Bulk DMI was implemented via the energy density

$$w_{DMI} = D\boldsymbol{m} \cdot \left(\frac{\partial \boldsymbol{m}}{\partial x} \times \boldsymbol{e}_x - \frac{\partial \boldsymbol{m}}{\partial y} \times \boldsymbol{e}_y\right) \quad (1)$$

where D is the DMI constant, $\boldsymbol{m}$ is the unit magnetization vector,[56] and $\boldsymbol{e}_x$ and $\boldsymbol{e}_y$ are the unit vector along x and y directions, respectively. The resulting effective field term contribution is included in the Landau-Lifshitz-Gilbert (LLG) equation as an additional field term besides exchange, demagnetization, uniaxial anisotropy, and Zeeman fields. The temperature material parameters are assumed to follow well-established laws[57,58] where the saturation magnetization is scaled with $M_s(T) = M_s(0)\left(1 - \frac{T}{T_C}\right)^{0.5}$, the exchange and anisotropy constants are scaled via $A_{ex}(T) = A(0)\left(\frac{M_s(T)}{M_s(0)}\right)^{1.53}$, and $K_u(T) = K_u(0)\left(\frac{M_s(T)}{M_s(0)}\right)^{1.85}$. For the material parameters at $T = 0$ K $M_s(0) = 900$ kA m^{-1}, $A_{ex}(0) = 30$ pJ m^{-1}, and $K_u(0) = 300$ kJ m^{-3} were used as appropriate choices based on experimental expectations, and previous publications.[26] The exchange and anisotropy constants were very difficult to measure based on the very small sizes of the single crystal sample. Hence, a comprehensive study not shown here was done, where initial parameters were optimized by investigating the size of an elliptical skyrmion and a square antiskyrmion, and matching them to experimental findings.

The stability of nano-objects was investigated by means of a finite-difference-method micromagnetic simulations using magnum.np.[44] A small geometry was discretized with lateral dimensions of $x = 300$, $y = 300$, and thickness $z = 280$ nm into cells with volume $d_x \times d_y \times d_z = 5 \times 5 \times 28$ nm^3. It was started from a rough parametrization of the aSk and eBSk. A small random vector was added in each cell to the magnetization to create a distorted magnetization state. The structure was then relaxed by numerically solving the LLG using temperature-dependent magnetic parameters. The strength of the DMI was varied as well to obtain the stability phase diagrams. The topological Skyrmion numbers are calculated via $N_{SK} = \frac{1}{4\pi} \iint \boldsymbol{m}(\boldsymbol{r}) \cdot \left(\frac{\partial \boldsymbol{m}(\boldsymbol{r})}{\partial x} \times \frac{\partial \boldsymbol{m}(\boldsymbol{r})}{\partial y}\right) d^2r$ and coded as the color in the phase diagrams. The topological charge was calculated by averaging the magnetization along the z-axis and then integrating N_{SK} as a volume integral. Finally, it was divided by the cell thickness along z, to approximate the surface integral.

Large-scale lattice simulations were performed on a geometry with lateral dimensions of $x = 3000$, $y = 3000$, and thickness $z = 280$ nm. The applied OOP field was varied, and the DMI strength to find stable lattice solutions for the eBSKs (stable lattice using $T_{eff} = 100$K, $D_{2d} = 1.8$ mJ m^{-2}, and

$B_z = 500$ mT), and aSK (stable lattice using $T_{eff} = 300$ K, $D_{2d} = 1.3$ mJ m^{-2}, and $B_z = 450$ mT). The stabilized lattices were then taken as initial magnetization states for the field-driven transformation simulations, where a time-dependent magnetic field decreases with a rate of 0.5 mT ns^{-1}.

The minimum energy paths were obtained via the full micromagnetic model using a string method,[47–49] using magnum.fe[59] which was similar to the nudged elastic band method[46] and delivers the energetically most favorable way to switch the initial magnetization state into a chosen final state based on the chosen initial path. The string method was iterative and consists of two steps in the main routine. The initial and final states were initially interpolated in an equidistant manner along an initial path into magnetization images. The first step consists of a local minimization process by using the steepest descent method for each magnetization image. In the second step, one interpolates the new energy curve into equidistant images on a new path using an appropriate energy norm. One repeats these two steps until the energy path describing the desired physical switching, or deformation does not change anymore. The converged curve was considered to be the minimum energy path. Note here that annihilation and deformation processes involving a Bloch point could be described qualitatively via micromagnetic simulations, yet the obtained energy barriers could be significantly underestimated,[60] as micromagnetics was not suitable for the modeling of Bloch points.

Supporting Information

Supporting Information is available from the Wiley Online Library or from the author.

Acknowledgements

Conflict of Interest

The authors declare no conflict of interest.

Author Contributions

J.J. and S.K. contributed equally to the work. J.J. and S.S.P.P. conceived the project. C.F. provided the bulk material. J.J. performed the EBSD and Lorentz TEM experiments. J.J. analyzed the experimental data and K.H. and M.T. contributed to the analysis. S.K., F.B., and C.A. wrote and improved the micromagnetic simulation code. S.K. performed the micromagnetic simulations under the supervision of C.A. and D.S. J.J., S.K., D.S., and S.S.P.P. wrote the manuscript. S.S.P.P. supervised the project. All authors participated in discussing the data and drafting the manuscript.

Data Availability Statement

The data that support the findings of this study are available from the corresponding author upon reasonable request.

Keywords

[1] A. Bogdanov, A. Hubert, *J. Magn. Magn. Mater.* **1994**, *138*, 255.
[2] A. Fert, V. Cros, J. Sampaio, *Nat. Nanotechnol.* **2013**, *8*, 152.
[3] S. S. Parkin, M. Hayashi, L. Thomas, *Science* **2008**, *320*, 190.
[4] X. Zhang, M. Ezawa, Y. Zhou, *Sci. Rep.* **2015**, *5*, 9400.
[5] S. Mühlbauer, B. Binz, F. Jonietz, C. Pfleiderer, A. Rosch, A. Neubauer, R. Georgii, P. Böni, *Science* **2009**, *323*, 915.
[6] X. Yu, Y. Onose, N. Kanazawa, J. Park, J. Han, Y. Matsui, N. Nagaosa, Y. Tokura, *Nature* **2010**, *465*, 901.
[7] X. Yu, N. Kanazawa, Y. Onose, K. Kimoto, W. Zhang, S. Ishiwata, Y. Matsui, Y. Tokura, *Nat. Mater.* **2011**, *10*, 106.
[8] S. Seki, X. Yu, S. Ishiwata, Y. Tokura, *Science* **2012**, *336*, 198.
[9] I. Kézsmárki, S. Bordács, P. Milde, E. Neuber, L. Eng, J. White, H. M. Rønnow, C. Dewhurst, M. Mochizuki, K. Yanai, *Nat. Mater.* **2015**, *14*, 1116.
[10] T. Kurumaji, T. Nakajima, V. Ukleev, A. Feoktystov, T.-h. Arima, K. Kakurai, Y. Tokura, *Phys. Rev. Lett.* **2017**, *119*, 237201.
[11] A. K. Nayak, V. Kumar, T. Ma, P. Werner, E. Pippel, R. Sahoo, F. Damay, U. K. Rößler, C. Felser, S. S. Parkin, *Nature* **2017**, *548*, 561.
[12] J. Jena, R. Stinshoff, R. Saha, A. K. Srivastava, T. Ma, H. Deniz, P. Werner, C. Felser, S. S. Parkin, *Nano Lett.* **2020**, *20*, 59.
[13] K. Karube, L. Peng, J. Masell, X. Yu, F. Kagawa, Y. Tokura, Y. Taguchi, *Nat. Mater.* **2021**, *20*, 335.
[14] C. Moreau-Luchaire, C. Moutafis, N. Reyren, J. Sampaio, C. Vaz, N. Van Horne, K. Bouzehouane, K. Garcia, C. Deranlot, P. Warnicke, *Nat. Nanotechnol.* **2016**, *11*, 444.
[15] O. Boulle, J. Vogel, H. Yang, S. Pizzini, D. de Souza Chaves, A. Locatelli, T. O. Menteş, A. Sala, L. D. Buda-Prejbeanu, O. Klein, *Nat. Nanotechnol.* **2016**, *11*, 449.
[16] N. Nagaosa, Y. Tokura, *Nat. Nanotechnol.* **2013**, *8*, 899.
[17] B. Göbel, I. Mertig, O. A. Tretiakov, *Phys. Rep.* **2021**, *895*, 1.
[18] J. Jena, B. Göbel, T. Hirosawa, S. A. Díaz, D. Wolf, T. Hinokihara, V. Kumar, I. Mertig, C. Felser, A. Lubk, *Nat. Commun.* **2022**, *13*, 2348.
[19] A. Bogdanov, U. Rößler, M. Wolf, K.-H. Müller, *Phys. Rev. B* **2002**, *66*, 214410.
[20] J. Sampaio, V. Cros, S. Rohart, A. Thiaville, A. Fert, *Nat. Nanotechnol.* **2013**, *8*, 839.
[21] F. N. Rybakov, A. B. Borisov, S. Blügel, N. S. Kiselev, *New J. Phys.* **2016**, *18*, 045002.
[22] M. Heigl, S. Koraltan, M. Vaňatka, R. Kraft, C. Abert, C. Vogler, A. Semisalova, P. Che, A. Ullrich, T. Schmidt, *Nat. Commun.* **2021**, *12*, 2611.
[23] S. Montoya, S. Couture, J. Chess, J. Lee, N. Kent, D. Henze, S. Sinha, M.-Y. Im, S. Kevan, P. Fischer, *Phys. Rev. B* **2017**, *95*, 024415.
[24] T. Ma, A. K. Sharma, R. Saha, A. K. Srivastava, P. Werner, P. Vir, V. Kumar, C. Felser, S. S. Parkin, *Adv. Mater.* **2020**, *32*, 2002043.
[25] A. K. Srivastava, P. Devi, A. K. Sharma, T. Ma, H. Deniz, H. L. Meyerheim, C. Felser, S. S. Parkin, *Adv. Mater.* **2020**, *32*, 1904327.
[26] J. Jena, B. Göbel, T. Ma, V. Kumar, R. Saha, I. Mertig, C. Felser, S. S. Parkin, *Nat. Commun.* **2020**, *11*, 1115.
[27] L. Peng, R. Takagi, W. Koshibae, K. Shibata, K. Nakajima, T.-h. Arima, N. Nagaosa, S. Seki, X. Yu, Y. Tokura, *Nat. Nanotechnol.* **2020**, *15*, 181.
[28] J. Jena, B. Göbel, V. Kumar, I. Mertig, C. Felser, S. Parkin, *Sci. Adv.* **2020**, *6*, abc0723.
[29] T. Graf, C. Felser, S. S. Parkin, *Prog. Solid State Chem.* **2011**, *39*, 1.

ADVANCED
SCIENCE NEWS

www.advancedsciencenews.com

ADVANCED
FUNCTIONAL
MATERIALS

www.afm-journal.de

[30] A. J. Wilkinson, T. B. Britton, *Mater. Today* **2012**, *15*, 366.

[31] A. J. Schwartz, M. Kumar, B. L. Adams, D. P. Field, *Electron Backscatter Diffraction in Materials Science*, Vol. 2, Springer, New York, **2009**.

[32] V. Kumar, N. Kumar, M. Reehuis, J. Gayles, A. Sukhanov, A. Hoser, F. Damay, C. Shekhar, P. Adler, C. Felser, *Phys. Rev. B* **2020**, *101*, 014424.

[33] M. Potkina, I. Lobanov, O. Tretiakov, H. Jónsson, V. Uzdin, *Phys. Rev. B* **2020**, *102*, 134430.

[34] M. Ezawa, *Phys. Rev. B* **2011**, *83*, 100408.

[35] X. Liang, L. Shen, X. Xing, Y. Zhou, *Commun. Phys.* **2022**, *5*, 310.

[36] U. Güngördü, S. Sandhoefner, A. A. Kovalev, *Phys. Rev. B* **2018**, *97*, 115136.

[37] X. Yu, D. Morikawa, T. Yokouchi, K. Shibata, N. Kanazawa, F. Kagawa, T.-h. Arima, Y. Tokura, *Nat. Phys.* **2018**, *14*, 832.

[38] Y.-Y. Dai, H. Wang, T. Yang, A. O. Adeyeye, Z.-D. Zhang, *Rare Met.* **2022**, *41*, 3150.

[39] P.-J. Hsu, A. Kubetzka, A. Finco, N. Romming, K. Von Bergmann, R. Wiesendanger, *Nat. Nanotechnol.* **2017**, *12*, 123.

[40] K. Zeissler, S. Finizio, C. Barton, A. J. Huxtable, J. Massey, J. Raabe, A. V. Sadovnikov, S. A. Nikitov, R. Brearton, T. Hesjedal, *Nat. Commun.* **2020**, *11*, 428.

[41] F. S. Yasin, J. Masell, K. Karube, A. Kikkawa, Y. Taguchi, Y. Tokura, X. Yu, *Proc. Natl. Acad. Sci. USA* **2022**, *119*, 2200958119.

[42] K. Litzius, J. Leliaert, P. Bassirian, D. Rodrigues, S. Kromin, I. Lemesh, J. Zazvorka, K.-J. Lee, J. Mulkers, N. Kerber, *Nat. Electron.* **2020**, *3*, 30.

[43] H. Du, R. Che, L. Kong, X. Zhao, C. Jin, C. Wang, J. Yang, W. Ning, R. Li, C. Jin, *Nat. Commun.* **2015**, *6*, 8504.

[44] F. Bruckner, S. Koraltan, C. Abert, D. Suess, *Sci. Rep.* **2023**, *13*, 12054.

[45] A. K. Sharma, J. Jena, K. G. Rana, A. Markou, H. L. Meyerheim, K. Mohseni, A. K. Srivastava, I. Kostanoskiy, C. Felser, S. S. Parkin, *Adv. Mater.* **2021**, *33*, 2101323.

[46] L. Desplat, J.-V. Kim, R. Stamps, *Phys. Rev. B* **2019**, *99*, 174409.

[47] E. Weinan, W. Ren, E. Vanden-Eijnden, *J. Chem. Phys.* **2007**, *126*, 164103.

[48] C. Abert, *Eur. Phys. J. B* **2019**, *92*, 120.

[49] S. Koraltan, M. Pancaldi, N. Leo, C. Abert, C. Vogler, K. Hofhuis, F. Slanovc, F. Bruckner, P. Heistracher, M. Menniti, *Phys. Rev. B* **2020**, *102*, 064410.

[50] A. V. Chumak, P. Kabos, M. Wu, C. Abert, C. Adelmann, A. Adeyeye, J. Åkerman, F. G. Aliev, A. Anane, A. Awad, *IEEE Trans. Magn.* **2022**, *58*, 6.

[51] C. Felser, A. Hirohata, *Heusler Alloys*, Vol. 222, Springer, Cham, **2016**.

[52] Z. Wang, H. Yuan, Y. Cao, Z.-X. Li, R. A. Duine, P. Yan, *Phys. Rev. Lett.* **2021**, *127*, 037202.

[53] D. Pinna, G. Bourianoff, K. Everschor-Sitte, *Phys. Rev. Appl.* **2020**, *14*, 054020.

[54] G. Bourianoff, D. Pinna, M. Sitte, K. Everschor-Sitte, *AIP Adv.* **2018**, *8*, 055602.

[55] R. Msiska, J. Love, J. Mulkers, J. Leliaert, K. Everschor-Sitte, *Adv. Intell. Syst.* **2023**, *5*, 2200388.

[56] D. Cortés-Ortuño, M. Beg, V. Nehruji, L. Breth, R. Pepper, T. Kluyver, G. Downing, T. Hesjedal, P. Hatton, T. Lancaster, *New J. Phys.* **2018**, *20*, 113015.

[57] R. Moreno, R. Evans, S. Khmelevskyi, M. Muñoz, R. Chantrell, O. Chubykalo-Fesenko, *Phys. Rev. B* **2016**, *94*, 104433.

[58] W. Scholz, T. Schrefl, J. Fidler, *J. Magn. Magn. Mater.* **2001**, *233*, 296.

[59] C. Abert, L. Exl, F. Bruckner, A. Drews, D. Suess, *J. Magn. Magn. Mater.* **2013**, *345*, 29.

[60] P. Heistracher, C. Abert, F. Bruckner, C. Vogler, D. Suess, *IEEE Trans. Magn.* **2018**, *54*, 7206105.